Cart3D Simulations for the First AIAA Sonic Boom Prediction Workshop

Michael J. Aftosmis*
NASA Ames, Moffett Field, CA 94035

Marian Nemec†
Science & Technology Corp., Moffett Field, CA 94035

Simulation results for the First AIAA Sonic Boom Prediction Workshop (LBW1) are presented using an inviscid, embedded-boundary Cartesian mesh method. The method employs adjoint-based error estimation and adaptive meshing to automatically determine resolution requirements of the computational domain. Results are presented for both mandatory and optional test cases. These include an axisymmetric body of revolution, a 69° delta wing model and a complete model of the Lockheed N+2 supersonic tri-jet with V-tail and flow through nacelles. In addition to formal mesh refinement studies and examination of the adjoint-based error estimates, mesh convergence is assessed by presenting simulation results for meshes at several resolutions which are comparable in size to the unstructured grids distributed by the workshop organizers. Data provided includes both the pressure signals required by the workshop and information on code performance in both memory and processing time. Various enhanced techniques offering improved simulation efficiency will be demonstrated and discussed.

I. Introduction

Analysis methods for sonic boom prediction have improved dramatically in recent years as a result of both commercial and government interest in overland supersonic flight. Backed by programatic investment within NASA and elsewhere, a number of simulation tools have recently become available for predicting high-fidelity pressure signals several body lengths away from an aircraft.[1–11] At such distances, details of the three-dimensional aircraft geometry become less important and atmospheric propagation codes[12–14] can be employed to model wave propagation through the atmosphere and to the ground.

While several technologies have played roles in improving the effectiveness of CFD-based analysis, one of the keys has been the widespread use of adaptive mesh techniques.[1–4,6,7,15–17] Configurations designed for low sonic-boom necessarily send only weak pressure disturbances toward the ground. Accurate propagation of such weak waves over several body lengths is a challenge for any numerical simulation technique. Adaptive meshing techniques concentrate and orient mesh elements in the computational domain to more efficiently propagate these signals and have been far more successful than earlier efforts. Particularly noteworthy has been the contribution of adjoint equation or output-based meshing approaches which can prioritize mesh refinement specifically to annihilate error in the propagated signal.[3,4,6,16,18] The insight provided by these approaches has benefitted even fixed-mesh approaches since they aid in our understanding of flow sensitivities, meshing requirements and the role of discretization error in these simulations.

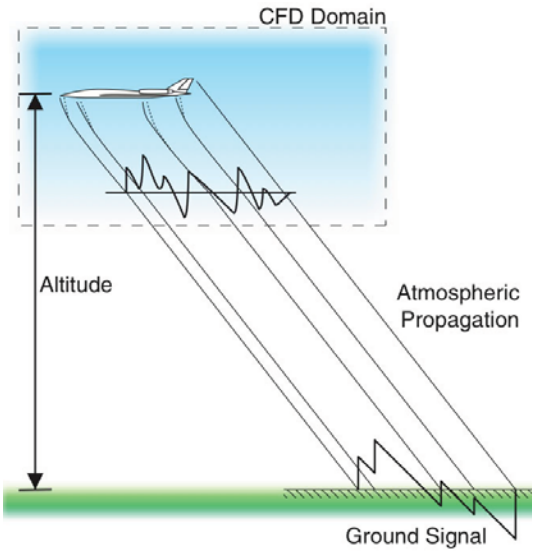

Figure 1. Sketch of basic methodology used for sonic boom prediction with CFD.

*Aerospace Engineer, *michael.aftosmis@nasa.gov* Associate Fellow AIAA.
†Senior Research Scientist, *marian.nemec@nasa.gov* Member AIAA.

The objective of the first sonic-boom prediction workshop is to document the state of the art for prediction of near-field pressure signatures and gain an understanding of modeling requirements for accurate and reliable sonic boom prediction.[19] To facilitate direct comparison, the workshop organizers provide both CAD geometry as well as surface and volume grids for structured, unstructured (tetrahedral) and mixed-element grids. Workshop participants were requested to apply their best practices for computing solution on the provided geometries. In addition, there was particular interest in exploring refinement techniques including grid adaptation and alignment with flow characteristics.

Given their specialization, Cartesian meshes were not included in the grid-sets provided by the organizing committee. Despite this, simulations using embedded-boundary Cartesian grids are quite common used within the low-boom design community. The Cart3D simulation package with the Adjoint ERror mesh Optimization (AERO) module is employed for low-boom simulations within NASA at the Langley, Glen and Ames research centers, it is also broadly employed across various industrial and academic members of the low-boom community. Cartesian methods have been of interest since at least the 2008 NASA Fundamental Aeronautics Low Boom Workshop[20] and many of the specialized techniques commonly used for such computations were pioneered on these grids.[4] While Cartesian grids were not distributed *per-se*, surface representations (either CAD or unstructured surface triangulations) were provided and these descriptions provided the geometric models for this work. Meshes used in this work were chosen to roughly correspond to the resolution levels provided for other meshing topologies considered by the workshop organizers for the various problems.

At present, the organizing committee has not yet released final versions of all the geometries to be considered in this workshop. Preliminary results included herein reflect this in that (1) the Body of Revolution is not yet final, (2) experimental data from the 2012 testing of the delta-wing-body has not been released and (3) and the complete aircraft geometry while very similar, is different from that which will be studied by the workshop.

II. Background and Method

In early 2008, Nemec, Aftosmis, and Wintzer[3] used embedded-boundary Cartesian meshing along with adjoint-based mesh adaptation to predict the pressure signature due to a diamond airfoil in supersonic flow. This work used both an off-body functional to drive the adjoint and introduced a mesh alignment technique based on the mach-angle of the free-stream flow. The capability was built upon a preexisting mesh adaptation scheme[21] and adjoint solver.[22] Three dimensional examples using the Cartesian-adjoint approach were presented in June 2008[4] and the method was subsequently used to participate in the 2008 NASA Fundamental Aeronautics Program Sonic Boom Prediction Workshop.[20]

The simulation package uses a Cartesian cut-cell approach[23] in which the governing equations are discretized on a multilevel Cartesian mesh with embedded boundaries. The mesh consists of regular Cartesian hexahedra everywhere, except for a layer of body-intersecting boundaries as illustrated in Fig. 1. The spatial discretization uses a second-order accurate finite volume method with a weak imposition of boundary conditions, resulting in a system of equations

$$R(Q_H) = 0 \tag{1}$$

The flux-vector splitting approach of van Leer[24] is used for residual evaluation. Although it consists of nested Cartesian cells, the mesh is viewed as an unstructured collection of control volumes making the approach well-suited for solution-adaptive mesh refinement. Steady-state flow solutions are obtained using a five-stage Runge–Kutta scheme with local time stepping and multigrid. Domain decomposition via space-filling curves permits parallel computation; for more details see Aftosmis *et al.* and Berger *et al.*[25–27]

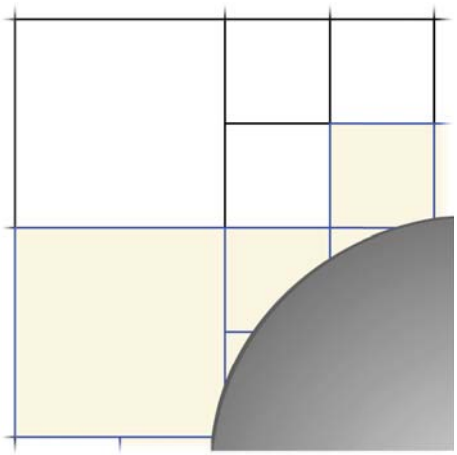

Figure 2. Multilevel Cartesian mesh in two-dimensions with a cut-cell boundary.

When applied to boom propagation problems, the Cartesian mesh is frequently rotated to roughly align the mesh cells with the free stream Mach-wave angle. This alignment also encourages cell stretching along

the dominant wave propagation direction to directly increase the per-cell signal propagation distance. Details of these techniques are discussed in Wintzer *et al.*[4]

In 2005, a duality-preserving discrete adjoint approach was introduced for Cart3D by Nemec and Aftosmis, this solver shares the same basic data structures, domain decomposition and other infrastructure with the primal solver and achieves similar performance.[22] While originally developed for gradient-based shape optimization,[28] the method was also employed for output error-estimation and adaptive mesh refinement[29] using an approach similar to that of Vendetti and Darmofal[30] and others.[31–33] This method was first applied directly to boom-propagation problems using an off-body field functional written as a pressure sensor with the quadratic form shown in eq.(2).[3]

$$\mathcal{J} = \int_0^L \frac{(p - p_\infty)^2}{p_\infty} dl \tag{2}$$

Integration of this functional is performed along a sensor of length L placed in the field where the signature is measured. With this functional output, the adjoint-based error-estimation then tailors the mesh refinement to reduce the error in the pressure signature at the location of the sensor. Error in this signal can be either driven below some pre-specified value, or alternatively, reduced as much as possible using a worst-errors-first strategy until a desired mesh size is reached. Adaptation is performed incrementally by cycling between the primal and adjoint solvers, with no more than one level of cell refinement being performed at a time. With this strategy, typical simulations cost 3-5 times that of a single flow solution on the final mesh.

Sonic boom problems are characterized by solutions with strong anisotropy at distances far from the body. This offers an opportunity to increase meshing efficiency by taking into consideration the anisotropy of the underlying flow physics. In Ref. [34] we introduced a technique for obtaining mesh stretching through anisotropic subdivision of cells in the Cartesian mesh. While this earlier work focused on vortex propagation over the long distances associated with formation flight, similar anisotropy exists in boom-propagation. *The final paper will show how this same technique can be applied in combination with adaptation to further reduce the computational expense of boom-propagation problems.*

III. Numerical Investigations

Simulations for the LBW1 workshop focuses on flow over three geometries. The simplest model is a body of revolution about 8 in. long that was constructed by the Boeing Company and tested in the NASA Ames 9×7 ft. supersonic tunnel in 2012. Data for this body was taken at Mach 1.6 at distances of 26-34 in. from the centerline. In addition, two lifting configurations were also considered, the first is a 69° delta-wing-body originally tested in the same tunnel in 1973,[35] but was recently re-tested using a newly developed pressure-rail and modern test techniques.[36,37] The final configuration was an optional exercise for boom prediction from a complete lifting supersonic transport configuration with flow-through nacelles. This geometry was developed by Lockheed Martin as part of a design study of "N+2" configurations for the NASA Fundamental Aeronautics Program's High-Speed Project.[38]

A. Case 1 – Body of Revolution

At the time of this writing, the organizing committee has not yet released the final geometry for the body-of-revolution test case. In order to demonstrate simulation capability for this abstract we're including analysis of a geometry similar to that planned for the workshop, at measurement distances comparable to those planned, and with data extracted at several different azimuthal locations

Our goal is to demonstrate accurate signal propagation off-track as well as directly on-track. This requires an understanding of the numerical scheme's behavior for sensors placed at various azimuths. To minimize computational expense, our meshing strategy aligns the Cartesian mesh with the characteristic wave propagation direction of the freestream by rotating the computational domain.[4,8] Since mesh cells are both aligned and stretched along the Mach angle of the oncoming supersonic flow, this meshing strategy clearly promotes propagation of signals from the geometry to sensors located on-track. The efficacy of this approach for sensors located at other azimuthal locations, however, is less obvious and warrants investigation.

To investigate numerical accuracy for such off-track signals, we perform a simple verification study using an axisymmetric model and examine signal propagation to an array of sensors located both on-track and

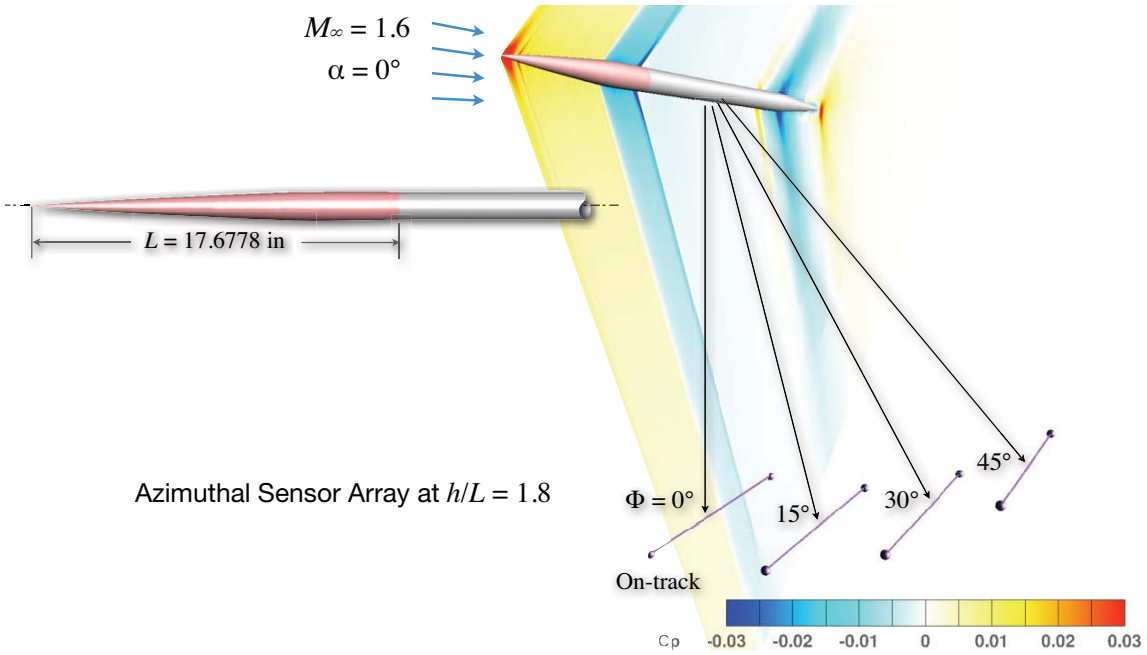

Figure 3. Axisymmetric geometry for workshop case 1. Pressure sensors are located at a distance $h/L = 1.8$ and at azimuthal locations $\Phi = \{0°, 15°, 30°, 45°\}$. $M_\infty = 1.6$, $\alpha = 0°$.

off-track. Figure 3 shows the model and problem setup. The model is a body of revolution based upon the work of Darden, George and Seebass,[39,40] but incorporating lift relaxation near the aft portion of the shape.[a] The axisymmetric model is mounted on a cylindrical sting which tapers to a point downstream. Symmetry dictates that when the body is aligned with the freestream ($\alpha = 0°$), the flowfield is axisymmetric and identical signals should be measured at sensors located at any azimuthal position. This symmetry provides an ideal basis for a verification exercise in which four sensors are placed in the simulation at azimuthal locations $\Phi = \{0°, 15°, 30°, 45°\}$, with the convention that on-track is at $\Phi = 0°$. The body length, L, is 17.678 inches and the sensors were all located a radial distance $h/L = 1.8$ away from the centerline.

Mesh adaptation is driven by a the sum of sensor functionals from Eq. 2 with identical weights placed on sensors at all azimuths.

$$\mathcal{J} = \frac{1}{p_\infty^2} \sum_{\Phi} \int (p - p_\infty)^2 dS_\Phi \tag{3}$$

By comparing the off-track results with the on-track signal, we can quantify the scheme's performance at non-zero azimuths. Note that the output functional weighs errors along each of the four sensors equally. As a result, the adjoint-driven refinement scheme will attempt to equalize error contributions of each sensor by performing more adaptation near sensors that contribute higher error. Thus, the numerical experiment will also yield the resolution requirements to obtain equal error in off-track and on-track signals.

Figure 4 provides an overview of the mesh and flow solution at $M_\infty = 1.6$ and $\alpha = 0°$. The figure shows symmetry plane and perspective view with mesh cuts shaded by pressure coefficient. The initial mesh in this simulation contained ~10k cells. After 11 cycles of adaptive refinement this mesh had grown to nearly 13M cells (Fig. 4). The view in the symmetry plane shows the $\Phi = 0°$ sensor below the body and the expected pattern of mesh adaptation bounded in front by the cone-shock and in the rear by the last set of flow characteristics which impact the sensor. The flow over the forebody is essentially conical opening downstream, and the characteristics affecting the sensors are also conical but opening upstream. In this supersonic flow, the adjoint-based refinement roughly concentrates cells within the intersections of these cones. Planes cutting in crossflow directions pick-out conic sections as well. The perspective view at the right of Fig. 4 has an inclined crossflow plane cut through the forebody flow capturing the parabolic expansion as it sweeps out toward the off-track sensor locations.

[a]This geometry was provided by Lockheed Martin Corp.

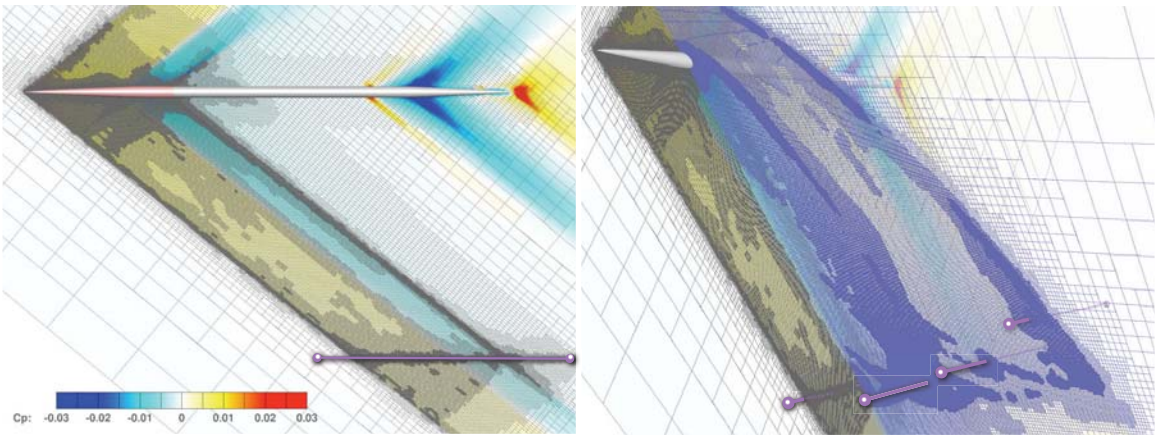

Figure 4. Symmetry plane (left) and perspective view (right) of cutting planes through the adaptively refined mesh used for workshop case 1. Sensors are located at $\Phi = \{0°, 15°, 30°, 45°\}$ a distance $h/L = 1.8$ from the body. The final mesh contains ~13M cells. $M_\infty = 1.6$, $\alpha = 0°$.

Figure 5 examines convergence of the functional (Eq. 3), its adjoint-based correction and error-estimate, as described in our earlier work.[3, 29] Recall in this case that the functional is the sum of the pressures along the sensors. Taken together, these plots give a strong indication of mesh convergence in the simulation, since changes in these pressures are vanishing as the mesh is refined. The frame at the left shows convergence of both the functional and its correction (*i.e.* the functional value if the mesh were uniformly refined). Both asymptote with mesh refinement. Moreover, the fact that the correction systematically leads the functional is evidence that the problem is well behaved. The frame at the right shows convergence of the adjoint-based estimate of the error in $\mathcal{J}$. After about 30k cells, this estimate decreases steadily indicating that the mesh refinement is systematically eliminating discretization error in the computational domain.

Figure 6 shows a comparison of the pressure signals ($\Delta p/p_\infty$) along all four sensors. Agreement between the sensors is excellent and symbols have been added to distinguish among the various lines. Since the mesh was refined in response to estimates of the discretization error, the number of cells along each gives an indication of the meshing requirements to equalize error at the sensor locations. Cell counts along the sensors at 0°, 15°, 30° and 45° are 898, 908, 984 and 1209, respectively. This distribution is roughly cosine-like in the azimuth angle.

B. Case 2 – Lifting Delta-Wing-Body

Originally identified as "Model 4" in the 1973 wind tunnel study by Hunton *et al.*, the 69° delta-wing-body shown in figure 7 is the simplest lifting configuration considered in the workshop. The figure shows isometric,

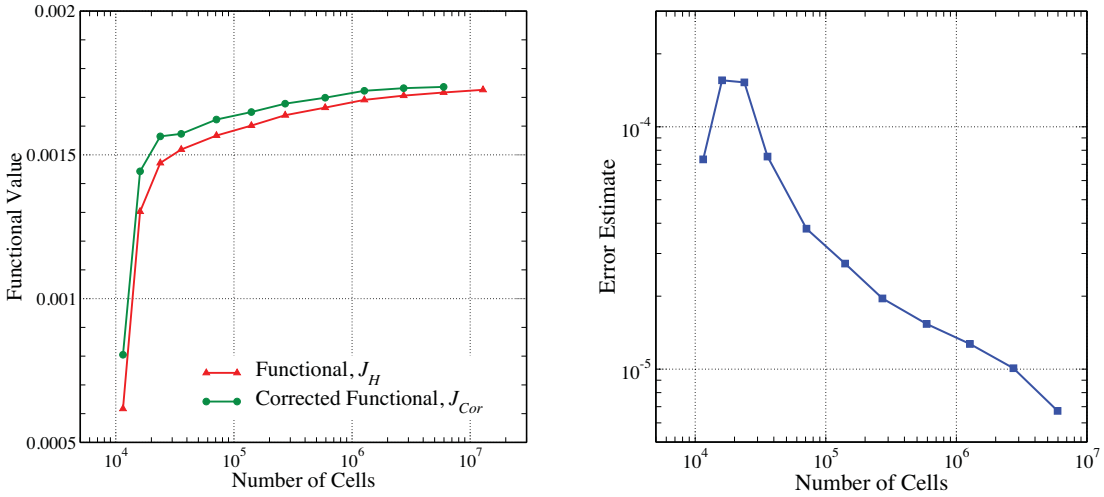

Figure 5. Mesh convergence of the functional (Eq. 3), its correction, and error-estimate for body of revolution in workshop case 1.

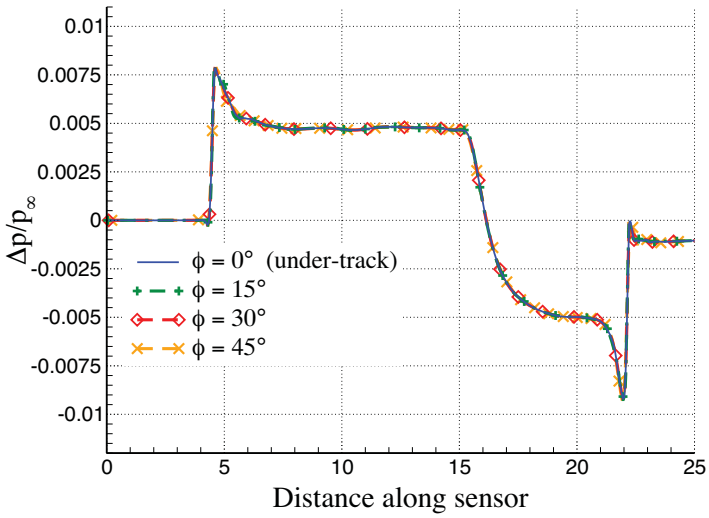

Φ	Num. Cells
0°	898
15°	908
30°	984
45°	1209

Figure 6. Case 1: Comparison of computed normalized pressure signals ($\Delta p/p_\infty$) on azimuthal sensor array shown in Fig. 3. The table at the right gives the final number of cells along the sensors at various azimuths.

planform and sectional views of this geometry which consists of a slender tangent-ogive-cylinder fuselage and a delta-wing with a 5% thick diamond airfoil. This geometry has been the subject of numerous numerical studies.[4,41,42] It was also one of the configurations studied by the NASA Fundamental Aeronautics workshop in 2008.[20]

In 2012, this model was re-tested in the NASA Ames 9×7 ft Unitary Plan supersonic tunnel using a newly developed pressure rail for instrumentation.[36] The workshop organizers plan to release on-track ($\Phi = 0°$) wind tunnel data from this recent test at distances between 21 inches and 32 inches. Off-track data will also be made available for Φ varying up 90°. At the 2008 workshop, various simulation codes used geometries which differed at the aft-end where the sting was attached (conical fairing vs. simple step-sting attachment) which seemed to be the source of slight differences in the results at particular h/L distances.[20] By providing a unified description of the geometry the current workshop and updated measurements will directly address this particular source of discrepancy.

Since the updated data is not available at the time of this writing, results in this section are presented along with the 1973 tunnel data and will be updated with the new run matrix and more recent data in the final paper.

Extracted pressure data from the 1973 tests[35] are available at several locations off body for various lift coefficients. Results in Figs. 8-10 were computed for $M_\infty = 1.68$ and $C_L = 0.15$. The desired lift coefficient

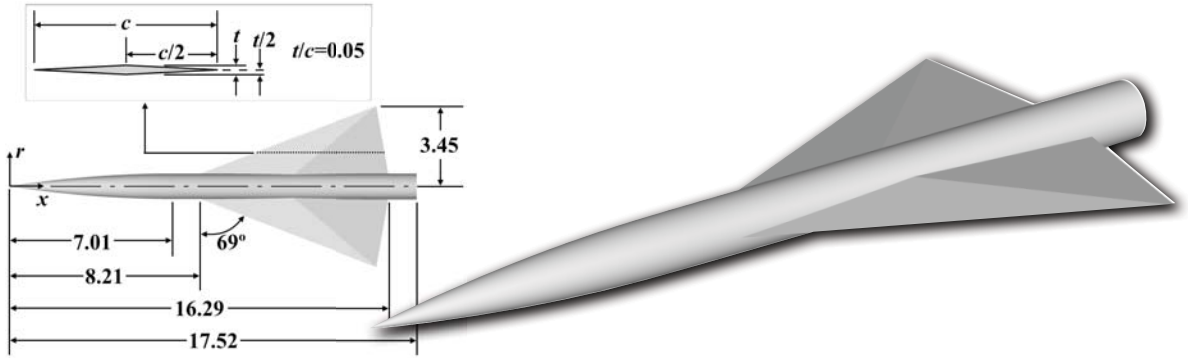

Figure 7. Planform, section and isometric views of the delta-wing-body from NASA TN-D 7160[35] used for workshop case 2.

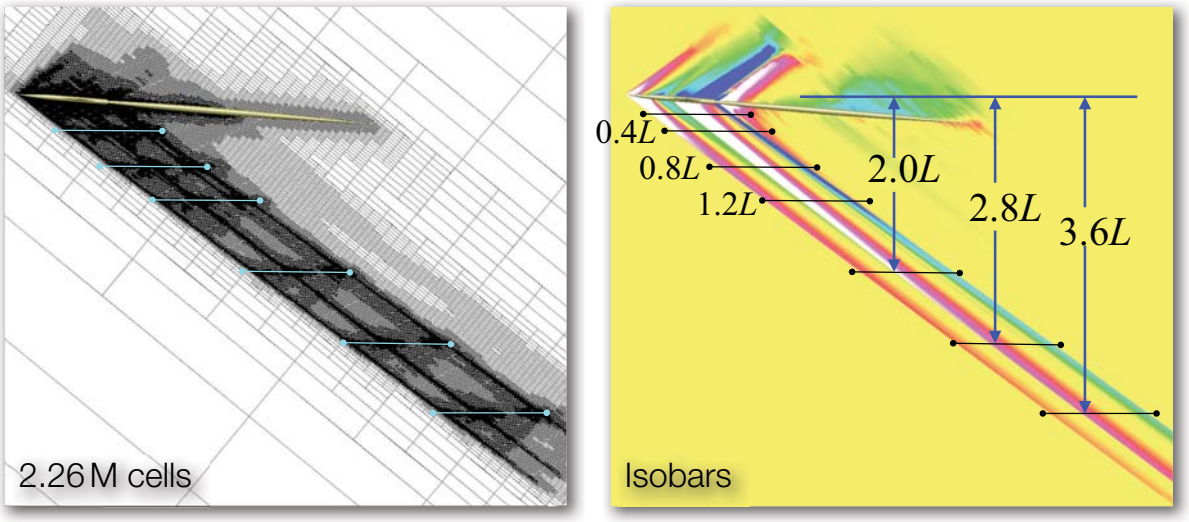

Figure 8. Case 2: Symmetry plane isobars and adapted Cartesian mesh for delta-wing-body at $M_\infty = 1.68$ and $C_L = 0.15$. Pressures were extracted at off-body distances of $h/L = \{0.2, 0.4, 0.8, 1.2, 2.0, 2.8, 3.6\}$. Adaptation for this example was driven using the functional shown in eq.(3), and the final mesh (shown) has 2.26 M cells.

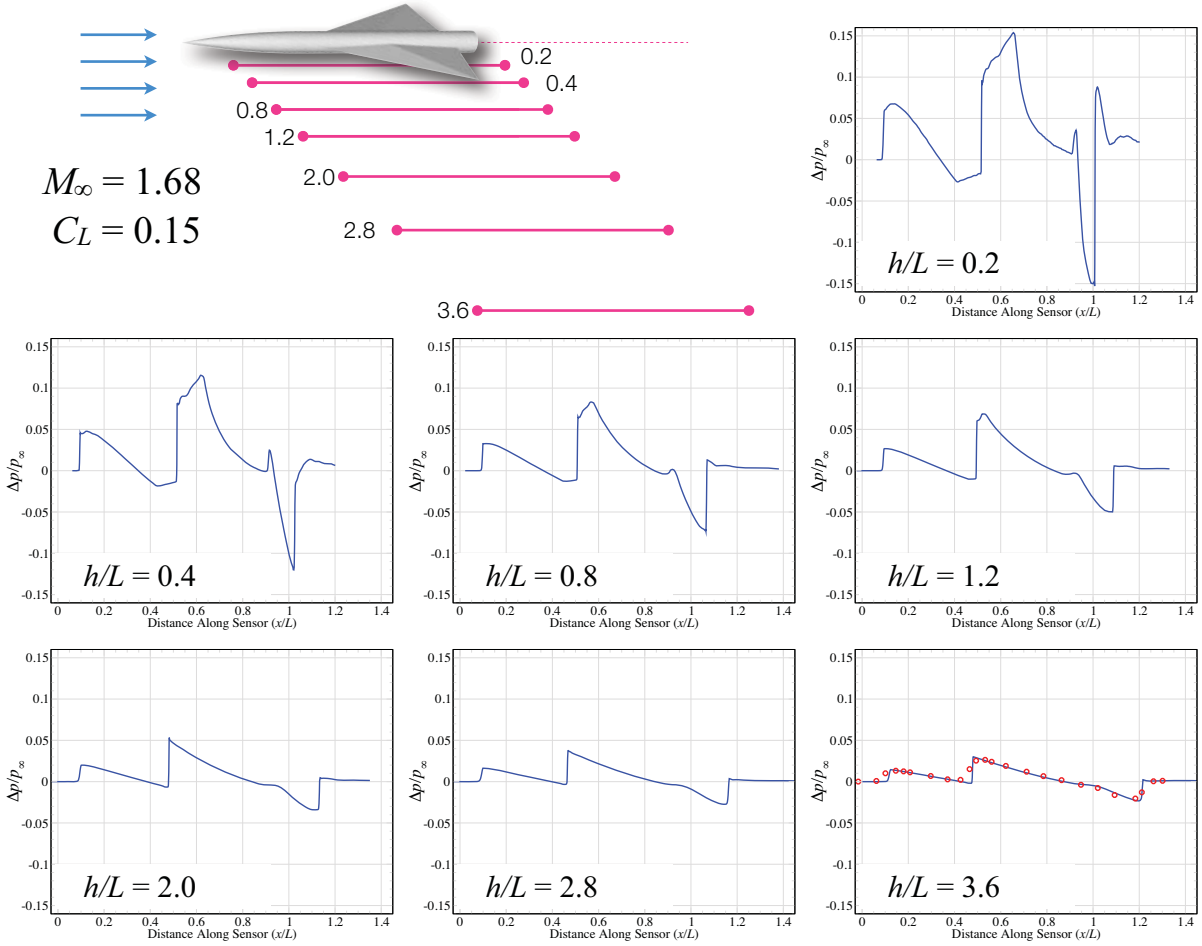

Figure 9. Case 2: On-track ($\Phi = 0°$) pressure signals for delta-wing-body geometry extracted from the simulation in fig.8. Pressures were extracted at off-body distances of $h/L = \{0.2, 0.4, 0.8, 1.2, 2.0, 2.8, 3.6\}$. Experimental data from Ref. [35] is included where available.

was achieved with a free stream angle-of-attack of 4.74°. Pressures were extracted at off-body distances of $h/L = \{0.2, 0.4, 0.8, 1.2, 2.0, 2.8, 3.6\}$. Adaptation for this example was driven using the functional shown in eq.(3). The final mesh is shown in Fig. 8 along with isobars in the discrete solution and the final mesh (shown) has 2.26 M cells.

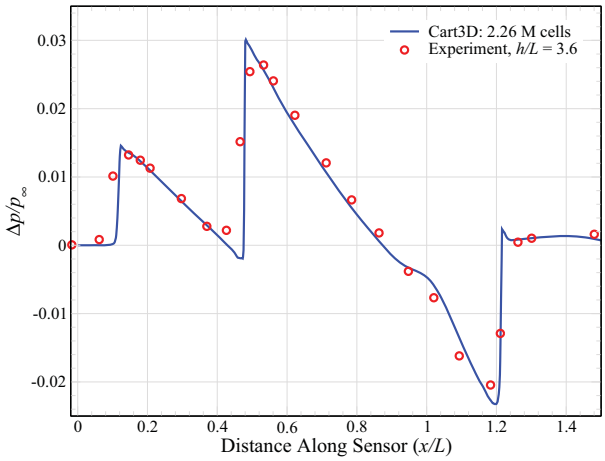

Figure 10. Comparison of computed pressure signal at $h/L = 3.6$ with experimental data from Ref. [35] at $M_\infty = 1.68$ and $C_L = 0.15$.

Figure 9 shows the pressure signal extracted the seven locations $h/L = \{0.2, 0.4, 0.8, 1.2, 2.0, 2.8, 3.6\}$ on an identically scaled set of thumbnail plots. This portrayal permits a clear depiction of the evolving signal as it weakens with increasing distance away from the body. Experimental data at this condition ($M_\infty = 1.68$ and $C_L = 0.15$) is available only at the final station ($h/L = 3.6$) as shown in the lower-right frame. Figure 10 contains an enlargement of this comparison showing very good agreement between the computational results and the experimental data.

C. Case 3 – Full Aircraft Configuration

The third case considered by the workshop was optional. This configuration was designed by Lockheed Martin Corp. and was tested jointly with NASA. Denoted "Configuration 12" this model was a full aircraft developed in Phase I of Fundamental Aeronautics' N+2 study.[38] Figure 11 shows CAD assembly drawings of the test article along with a table of key reference quantities. The low-boom tri-jet model included a fuselage, wing, V-tail, and included three, aft-mounted, flow through nacelles. The 0.8% scale model was 22.396 inches long and tested in the NASA Ames 9 × 7 ft Unitary Plan supersonic wind tunnel. On-track,

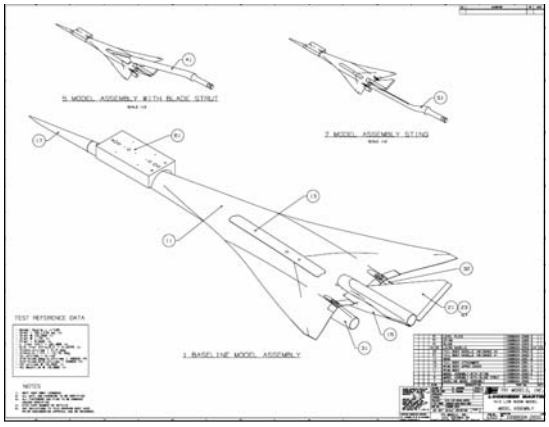

TEST REFERENCE DATA

Model Scale = 1/125
Sref = 33.1776 sq in
Xref @ 16.088 in
Zref @ 1.75 in
Cref @ 6.628 in
L (for H/L) = 22.396 in
b/2 (for H/[b/2]) = 4.027 in
Alpha_cruise = 2.3 deg
Alpha_0_lift = -0.75 deg
CL cruise = 0.142
Altitude_Begin_Cruise = 48500 ft
Altitude_End_Cruise = 54800 ft
CP cruise @ 16.590 in
AC Mach 1.6 @ 16.886 in

Figure 11. CAD drawings of full aircraft geometry tri-jet geometry designed by Lockheed Martin Corp. for workshop case 3 and tested in the NASA Ames 9 ×7 ft Unitary Plan supersonic tunnel in 2012.[38] Note both blade-sting and aft-sting configurations were tested. The table at the right includes reference quantities other engineering data for this configuration.

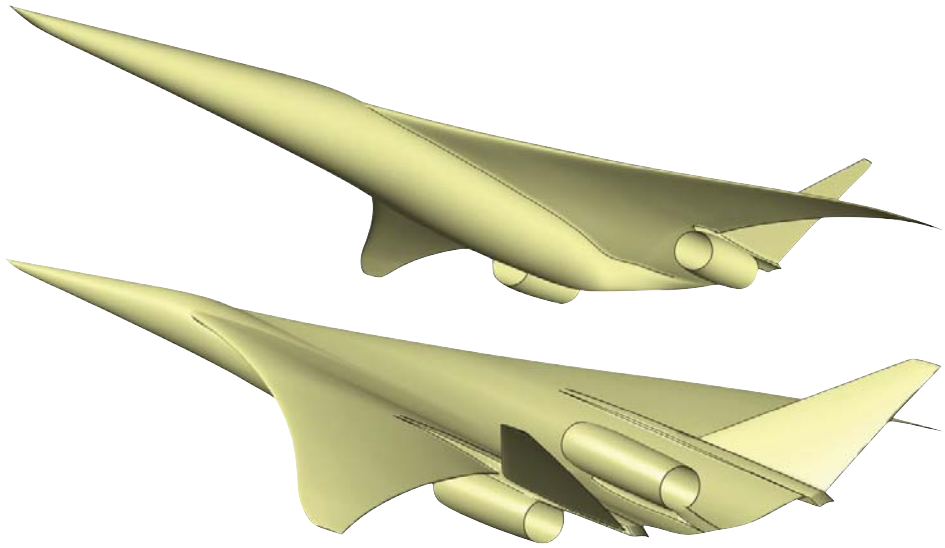

Figure 12. Front and rear 3/4 views of the full aircraft geometry used for case 3 simulations in this Extended Abstract. ***The actual workshop geometry for this case is shown in Fig. 11, but has not been released at the time of this writing, however the geometry shown here includes similar features including three flow-through nacelles.***

$\Phi = 0°$, pressures were measured 19.7 and 69.6 inches below the vehicle during testing. Some off-track data was also taken.

At the time of this writing, the organizing committee has not yet released the final geometry for this case. In order to demonstrate simulation capability for this abstract we're including analysis of a geometry similar to that planned for the workshop. In this abstract we only include on-track pressure signatures at only a single location.

Figure 13 contains a two views of the adapted computational mesh used for for signal propagation problem for the full aircraft simulation at $M_\infty = 1.7$. Adaptation was driven using a single pressure sensor located a distance of 2.08 body lengths directly below the vehicle ($h/L = 2.08$, $\Phi = 0°$).The top frame shows a close-up of the meshing near the body itself, while the lower is zoomed out to illustrate the relative position of the pressure sensor. This mesh has a total of ~11 M cells, and was created using 10 levels of adaptive refinement.

The final figure shows pressure along a sensor in discrete solution located on-track at a distance of $h/L = 2.08$ along with isobars in the simulation at $M_\infty = 1.7$. After a small shock at the nose, the pressure climbs nearly linearly before encountering shocks and expansions associated with the wing and nacelle. The evolution of these disturbances is evident in the isobars shown to the right. In boom propagation problems, stronger features such as these propagate faster than weak features such as the smooth compression near the nose. The isobars shown in this example illustrate this fact as the strong features near the middle of the sensor signal (approx. 175' down the sensor) actually emanate from the vicinity of the underwing nacelle and wing trailing edge. During propagation to the sensor, these waves have effectively migrated forward approximately 30% of the body length.

The workshop announcement requests data extraction from pressure sensors at 28 locations in the flow field around the "Configuration 12" geometry. The final paper will include all required pressure data and experimental comparisons for the correct optional geometry.

Summary

Since the final workshop geometries and/or comparison data have not been released at the time of this writing, this extended abstract included results for three similar models: (1) a simple body of revolution, (2) a 69° delta-wing-body and (3) a complete supersonic transport model with V-tail and flow through nacelles. These simulations illustrate the applicability of the embedded-boundary Cartesian mesh method to the analysis

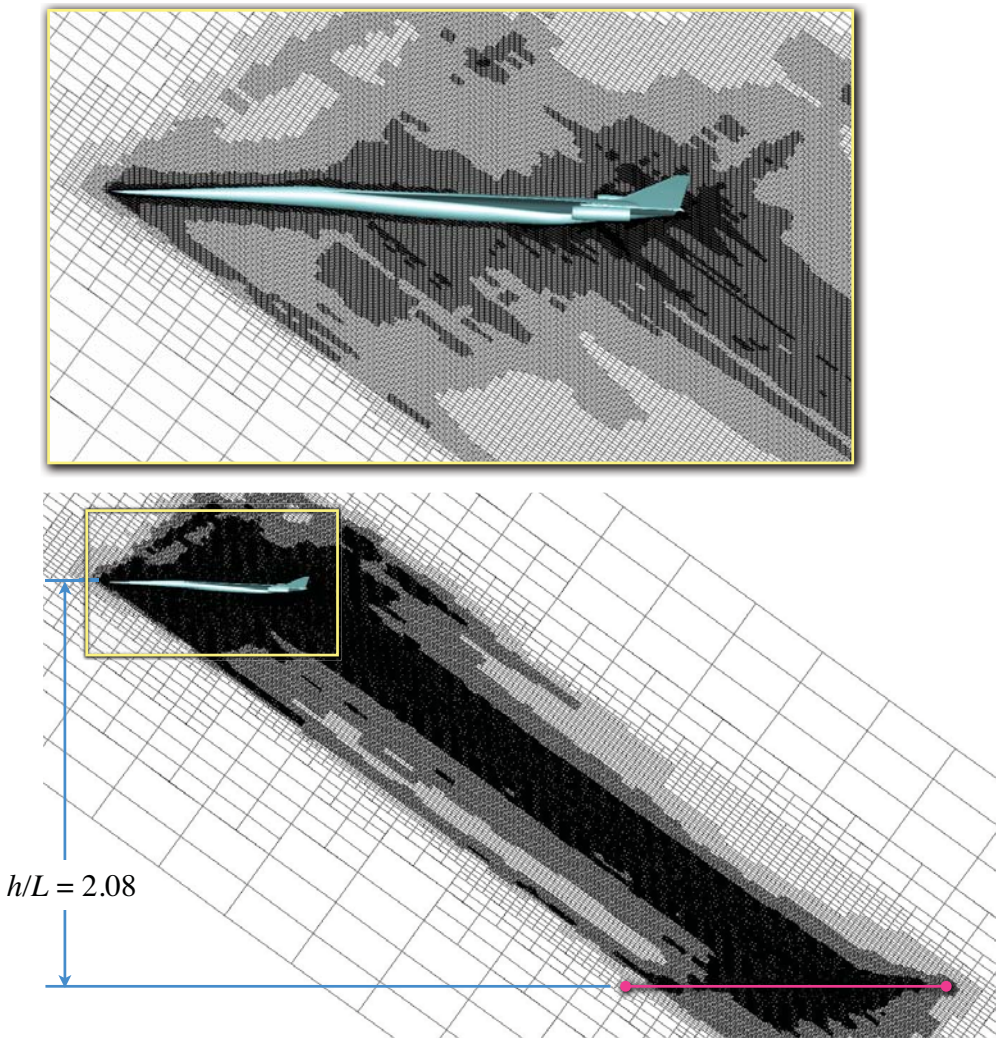

Figure 13. Adapted computational mesh used for for signal propagation problem for the full aircraft simulation of case 3 at $M_\infty = 1.7$. The sensor is located a distance of ~2.08 body lengths below the vehicle. This mesh has a total of 11 M cells, and was created using 10 levels of adaptive refinement.

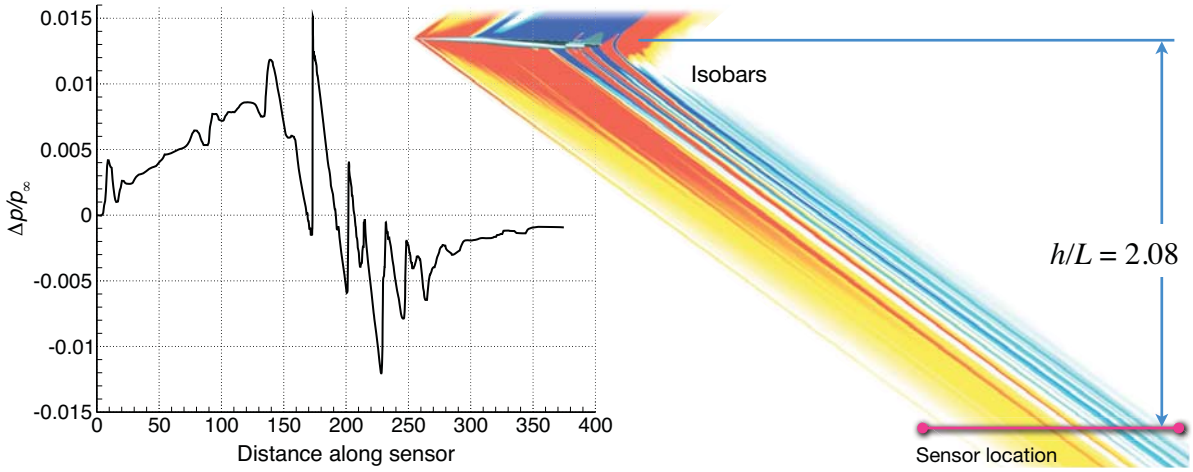

Figure 14. Case 3: Pressure along sensor located ~2.08 body lengths below full aircraft configuration for vehicle traveling at $M_\infty = 1.7$. The frame on the left shows the pressure as a function of distance along the sensor. To the right, isobars show pressure propagation in the discrete solution on the final adapted mesh (11 M cells).

and design of low sonic boom vehicles – especially when meshing is driven by adjoint-based error estimates. In addition to simulations around all required and optional geometries, the final paper will include studies of mesh convergence shown through functional convergence, convergence of the adjoint error-estimate and evolution of the off-body pressure signals. In addition, we will include information on code performance in both memory and processing time.

Acknowledgments

The authors wish to thank the members of the First AIAA Low Boom Workshop organizing committee for their superb effort and responsiveness throughout this work. This research was supported by the NASA Fundamental Aeronautics Program High-Speed project and by NASA Ames Research Center Contract NNA10DF26C. We are also grateful to Susan Cliff, David Rodriguez, and Mathias Wintzer for many useful discussions and generously sharing their insights into supersonic flight and boom prediction.

References

[1]Choi, S., Alonso, J. J., and Van der Weide, E., "Numerical and Mesh Resolution Requirements for Accurate Sonic Boom Prediction of Complete Aircraft Configurations," *AIAA Paper 2004–1060*, January 2004.

[2]Ozcer, I. A. and Kandil, O., "FUN3D/OptiGRID Coupling for Unstructrred Grid Adaptation for Sonic Boom Problems," *AIAA Paper 2008–0061*, January 2008.

[3]Nemec, M., Aftosmis, M. J., and Wintzer, M., "Adjoint-Based Adaptive Mesh Refinement for Complex Geometries," *AIAA Paper 2008-0725*, January 2008.

[4]Wintzer, M., Nemec, M., and Aftosmis, M. J., "Adjoint-Based Adaptive Mesh Renement for Sonic Boom Prediction," *AIAA Paper 2008–6593*, August 2008.

[5]Howe, D. C., "Hybrid Cart3D/OVERFLOW Near-Field Analysis of a Low Boom Configuration with Wind Tunnel Comparisons," *AIAA Paper 2011–3336*, June 2011.

[6]Park, M. A., "Low Boom Configuration Analysis with FUN3D Adjoint Simulation Framework," *AIAA Paper 2011–3337*, June 2011.

[7]Cliff, S. E., Elmiligui, A. A., Campbell, R., and Thomas, S. D., "Evaluation of Refined Tetrahedral Meshes with Projected, Stretched, and Sheared Prism Layers for Sonic Boom Analysis," *AIAA Paper 2011–3338*, June 2011.

[8]Nemec, M. and Aftosmis, M. J., "Parallel Adjoint Framework for Aerodynamic Shape Optimization of Component-Based Geometry," *AIAA Paper 2011–1249*, January 2011.

[9]Carter, M. B., Campbell, R., and Nayani, S., "USM3D Analysis of a Low Boom Configuration," *AIAA Paper 2011–3335*, June 2011.

[10]Alauzet, F. and Loseille, A., "High-Order Sonic Boom Modeling Based on Adaptive Methods," *Journal of Computational Physics*, Vol. 229, No. 3, 2010, pp. 561–593.

[11]Cliff, S. E., Thomas, S. D., McMullen, M., Melton, J. E., and Durston, D. A., "Assessment of Unstructured Euler Methods for Sonic Boom Pressure Signatures Using Grid Refinement and Domain Rotation Methods," NASA/TM 2008-214568, NASA, September 2008.

[12]Thomas, C., "Extrapolation of Sonic Boom Pressure Signatures by the Waveform Parameter Method," NASA TN-D-6832, June 1972.

[13]Durston, D. A., "A Preliminary Evaluation of Sonic Boom Extrapolation and Loudness Calculation Methods," *High-Speed Research: Sonic Boom*, NASA CP 10133, NASA Ames Research Center, May 12-14 1993, pp. 301–323.

[14]Rallabhandi, S. K., "Advanced Sonic Boom Prediction Using Augmented Burger's Equation," *AIAA Paper 2011–1278*, January 2011.

[15]Campbell, R., Carter, M. B., Deere, M., and Waithe, K. A., "Efficient Unstructured Grid Adaptation Methods for Sonic Boom Prediction," *AIAA Paper 2008–7327*, June 2008.

[16]Jones, W. T., Nielsen, E. J., and Park, M. A., "Validation of 3D Adjoint Based Error Estimation and Mesh Adaptation for Sonic Boom Prediction," AIAA Paper 2006–1150, Jan 2006.

[17]Kandil, O. and Ozcer, I. A., "Sonic Boom Computations for Double-Cone Configuration using CFL3D, FUN3D and Full-Potential Codes," *AIAA Paper 2006–0414*, January 2006.

[18]Alauzet, F., Dervieux, A., and Loseille, A., "Fully Anisotropic Goal-Oriented Mesh Adaptation for 3D Steady Euler Equations," *Journal of Computational Physics*, Vol. 229, No. 8, 2010, pp. 2866–2897.

[19]Waithe, K. A., "Introduction to the First Low Boom Prediction Workshop," *AIAA Paper 2013–0650*, Jan. 2013.

[20]Park, M. A., Aftosmis, M. J., Campbell, R. L., Carter, M. B., Cliff, S. E., and Bangert, L. S., "Summary of the 2008 NASA Fundamental Aeronautics Program Sonic Boom Prediction Workshop," *AIAA Paper 2013–0649*, Jan. 2013.

[21]Aftosmis, M. J. and Berger, M. J., "Multilevel Error Estimation and Adaptive h-Refinement for Cartesian Meshes with Embedded Boundaries," AIAA Paper 2002–0863, Reno, NV, Jan. 2002.

[22]Nemec, M., Aftosmis, M. J., Murman, S. M., and Pulliam, T. H., "Adjoint Formulation for an Embedded-Boundary Cartesian Method," AIAA Paper 2005–0877, Reno, NV, Jan. 2005.

[23]Aftosmis, M. J., Berger, M. J., and Melton, J. E., "Robust and Efficient Cartesian Mesh Generation for Componenet-Based Geometry," *AIAA Journal*, Vol. 36, No. 6, June 1998, pp. 952–960.

[24]van Leer, B., "Flux-Vector Splitting for the Euler Equations," ICASE Report 82-30, Sept. 1982.

[25]Aftosmis, M. J., Berger, M. J., and Adomavicius, G. D., "A Parallel Multilevel Method for Adaptively Refined Cartesian Grids with Embedded Boundaries," *AIAA-Paper 2000-0808*, Jan. 2000.

[26]Aftosmis, M. J., Berger, M. J., and Murman, S. M., "Applications of Space-Filling-Curves to Cartesian methods in CFD," *AIAA-Paper 2004-1232*, Jan. 2004.

[27]Berger, M. J., Aftosmis, M. J., and Murman, S. M., "Analysis of Slope Limiters on Irregular Grids," *AIAA Paper 2005–0490*, Jan. 2005.

[28]Nemec, M. and Aftosmis, M. J., "Adjoint Sensitivity Computations for an Embedded-Boundary Cartesian Mesh Method," *Journal of Computational Physics*, Vol. 227, 2008, pp. 2724–2742.

[29]Nemec, M. and Aftosmis, M. J., "Adjoint Error-Estimation and Adaptive Refinement for Embedded-Boundary Cartesian Meshes," *AIAA Paper 2007–4187*, June 2007.

[30]Venditti, D. A. and Darmofal, D. L., "Grid Adaptation for Functional Outputs: Application to Two-Dimensional Inviscid Flow," *Journal of Computational Physics*, Vol. 176, 2002, pp. 40–69.

[31]Becker, R. and Rannacher, R., "An Optimal Control Approach to a Posteriori Error Estimation in Finite Element Methods," *Acta Numerica 2000*, 2001, pp. 1–102.

[32]Giles, M. B. and Pierce, N. A., "Adjoint error correction for integral outputs," *Error Estimation and Adaptive Discretization Methods in Computational Fluid Dynamics*, edited by T. Barth and H. Deconinck, Vol. 25 of *Lecture Notes in Computational Science and Engineering*, Springer-Verlag, 2002.

[33]Barth, T., "Numerical Methods and Error Estimation for Conservation Laws on Structured and Unstructured Meshes," Lecture notes, von Karman Institute for Fluid Dynamics, Series: 2003-04, Brussels, Belgium, March 2003.

[34]Kless, J., Aftosmis, M. J., Ning, S. A., and Nemec, M., "Inviscid Analysis of Extended Formation Flight," *Seventh International Conference on Computational Fluid Dynamics (ICCFD7)*, Paper ICCFD7-4306, Big Island, Hawaii, June 2012.

[35]L. W., H., Hicks, R. M., and Mendoza, J. P., "Some Effects of Wing Planform on Sonic Boom," NASA TN-D-7160, National Aeronautics and Space Administration, January 1973.

[36]Cliff, S. E., Elmiligui, A. A., Aftosmis, M. J., Thomas, S. D., Morgenstern, J. M., and Durston, D. A., "Design and Evaluation of a Pressure Rail for Sonic Boom Measurement in Wind Tunnels," *Seventh International Conference on Computational Fluid Dynamics (ICCFD7)*, Paper ICCFD7-2006, Big Island, Hawaii, June 2012.

[37]Morgenstern, J. M., "How to Accurately Measure Low Sonic Boom or Model Surface Pressures in Supersonic Wind Tunnels," *AIAA Paper 2012–3215*, June 2012.

[38]Morgenstern, J. M., Buonanno, M., and Marconi, F., "Full Configuration Low Boom Model and Grids for 2014 Sonic Boom Prediction Workshop," *AIAA Paper 2013–0647*, Jan. 2013.

[39]Darden, C. M., "Sonic Boom Minimization with Nose-Bluntness," NASA-TP 1348, National Aeronautics and Space Administration, 1979.

[40]George, A. R. and Seabass, R., "Sonic Boom Minimization Including Both Front and Rear Shocks," *AIAA Journal*, Vol. 9, No. 10, 1971, pp. 2091–2093.

[41]Cliff, S. E. and Thomas, S. D., "Euler/Experiment Correlations of Sonic Boom Pressure Signatures," *Journal of Aircraft*, Vol. 30, No. 5, Sept.-Oct. 1993.

[42]Park, M. A. and Darmofal, D. L., "Output-Adaptive Tetrahedral Cut-Cell Validation for Sonic Boom Prediction,," *AIAA Paper 2008–6595*, August 2008.